


ARTICLE

<https://doi.org/10.1038/s41467-019-11970-8>

OPEN

Origin of synergistic effects in bicomponent cobalt oxide-platinum catalysts for selective hydrogenation reaction

Jiankang Zhang^{1,2}, Zhe Gao¹, Sen Wang¹, Guofu Wang¹, Xiaofeng Gao^{1,2}, Baiyan Zhang^{1,2}, Shuangfeng Xing^{1,2}, Shichao Zhao¹ & Yong Qin ^{1,2}

The synergistic nature of bicomponent catalysts remains a challenging issue, due to the difficulty in constructing well-defined catalytic systems. Here we study the origin of synergistic effects in CoO_x-Pt catalysts for selective hydrogenation by designing a series of closely contacted CoO_xPt/TiO₂ and spatially separated CoO_x/TiO₂/Pt catalysts by atomic layer deposition (ALD). For CoO_x/TiO₂/Pt, CoO_x and platinum are separated by the walls of titania nanotubes, and the CoO_x-Pt intimacy can be precisely tuned. Like CoO_xPt/TiO₂, the CoO_x/TiO₂/Pt shows higher selectivity to cinnamyl alcohol than monometallic TiO₂/Pt, indicating that the CoO_x-Pt nanoscale intimacy almost has no influence on the selectivity. The enhanced selectivity is ascribed to the increased oxygen vacancy resulting from the promoted hydrogen spillover. Moreover, platinum-oxygen vacancy interfacial sites are identified as the active sites by selectively covering CoO_x or platinum by ALD. Our study provides a guide for the understanding of synergistic nature in bicomponent and bifunctional catalysts.

¹State Key Laboratory of Coal Conversion, Institute of Coal Chemistry, Chinese Academy of Sciences, 27 Taoyuan South Road, 030001 Taiyuan, P.R. China.

²Center of Materials Science and Optoelectronics Engineering, University of Chinese Academy of Sciences, 100049 Beijing, P.R. China. Correspondence and requests for materials should be addressed to Z.G. (email: gaozhe@sxicc.ac.cn) or to Y.Q. (email: qinyong@sxicc.ac.cn)

Bicomponent catalysts have received considerably increasing interests in the recent decades due to the enhanced catalytic properties compared with their single-component counterparts, arising from direct contact between the two components, which can be called as synergistic effects^{1,2}. However, due to the limitations in controlling the catalyst microstructures and precisely tuning bicomponent intimacy by the traditional methods, it is still a challenging issue to understand the origin of synergistic effects (i.e., short- or long-range interactions) and identify the active sites.

The general belief is that the bicomponents should be as close as possible (i.e., short-range interactions of bicomponents) to promote electron interaction and/or construct interfaces to achieve effective catalysis. In this case, the interaction of a metal oxide promoter with a metal particle is puzzling due to the presence of multiple potential catalytic active sites under the reaction conditions. In contrast, some recent reports revealed the effects of intimacy on the catalyst performance when the bicomponents are separated and tuned at nanoscale and even millimeter-scale distance (i.e., long-range interactions of bicomponents)^{3–10}. For example, Coville and coworkers investigated the effect of Ru and Co intimacy on the activity and selectivity of Co catalysts using conventional incipient wetness impregnation in the typical Fischer–Tropsch reaction⁵. Bokhoven and coworkers prepared a series of model catalyst samples with precisely controlled Pt–FeO_x intimacy at nanoscale distances using the more precise nanolithography technique, and investigated the hydrogen spillover effects on TiO₂ and Al₂O₃ supports⁷. But no reaction (not possible for such structure) is conducted to verify the proposed hydrogen spillover mechanism under the real reaction conditions. Therefore, well-defined bicomponent catalytic systems are highly desirable to unravel the origin of synergistic effects under the real reaction conditions.

Atomic layer deposition (ALD) is a powerful thin-film technique for synthesis of conformal thin films and highly dispersed nanoparticles^{11–16}. Many advanced nanocatalysts have been designed and synthesized by ALD in the past decade^{17–26}. Herein, we investigate the effects of CoO_x–Pt intimacy on the selective hydrogenation of cinnamaldehyde (CALD) and the hydrogen spillover effects based on CoO_xPt/TiO₂ and well-designed spatially separated structures of CoO_x/TiO₂/Pt catalysts by a highly controllable and reliable ALD approach. Compared with the CoO_xPt/TiO₂, the CoO_x/TiO₂/Pt catalysts exhibit similar catalytic activity and hydrogenation selectivity for the CALD

hydrogenation, though the CoO_x–Pt intimacy of the two catalysts is dramatically different. This long-range promoter effect is not broken even when we selectively deposit additional coating layers on the CoO_x surfaces by ALD. The enhanced selectivity is ascribed to the promoted hydrogen spillover and thus increased oxygen vacancies (O_v). The well-designed structures can be synthesized and used to study the synergetic natures of other bicomponent and bifunctional catalysts with enhanced performance for other reactions.

Results

Synthesis and characterization of the catalysts. The closely contacted CoO_xPt/TiO₂ and spatially separated CoO_x/TiO₂/Pt catalysts were synthesized by a template-assisted ALD strategy (Fig. 1 and Supplementary Scheme 1)²⁶. For the synthesis of CoO_xPt/TiO₂, an amorphous TiO₂ film was first deposited on carbon nanocoils (CNCs) used as templates by ALD, obtaining TiO₂/CNCs, and then Pt nanoparticles were deposited on the TiO₂/CNCs by Pt ALD, obtaining Pt/TiO₂/CNCs. Subsequently, the CNCs were removed by calcination under an air atmosphere, producing Pt/TiO₂ catalysts with anatase nanotubes. Lastly, CoO_x nanoparticles were deposited on the outer surface of the Pt/TiO₂ through CoO_x ALD, producing CoO_xPt/TiO₂ catalysts with the closest CoO_x–Pt intimacy (Supplementary Scheme 1a). The CoO_x/TiO₂/Pt catalysts were prepared by exchanging the deposition sequence of TiO₂ and Pt (Supplementary Scheme 1b). The CoO_x–Pt intimacy can be precisely controlled by adjusting the thickness of TiO₂ layer. In addition, the CoO_x/TiO₂/Pt/TiO₂ and Al₂O₃/CoO_x/TiO₂/Pt catalysts (Fig. 1) were also prepared by selectively covering Pt with TiO₂ and CoO_x nanoparticles with Al₂O₃, respectively, to identify the real active sites in the bicomponent catalysts.

Figure 2 shows the transmission electron microscopy (TEM) and high-resolution TEM (HRTEM) images of the CoO_xPt/TiO₂ and CoO_x/TiO₂/Pt catalysts, prepared with 150, 20 and 300 cycles for CoO_x, Pt and TiO₂ deposition, respectively. The Pt and CoO_x nanoparticles, with average sizes of 2.9 nm and 4.3 nm, respectively (Supplementary Figs. 1 and 2), are highly dispersed on the outer surface of the anatase TiO₂ nanotubes with a wall thickness of ~13.7 nm, in which CoO_x is deposited on/next to Pt forming CoO_x–Pt interfaces (Fig. 2a, b). The measured lattice distances of the nanoparticles are ~0.223 nm and ~0.246 nm (Fig. 2b), which correspond to the Pt(111) and CoO (111) planes,

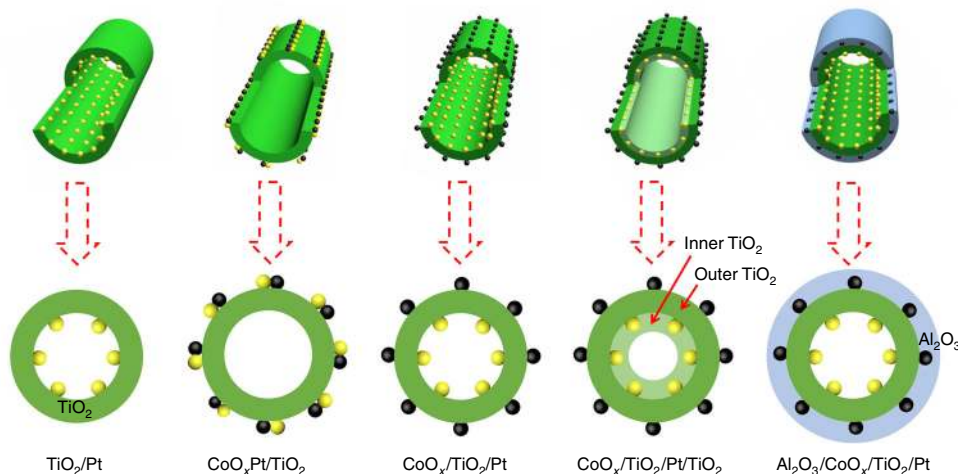


Fig. 1 Schematic illustration of the catalysts. Semi-sectional and cross-sectional views of the different catalysts prepared by ALD. The yellow and black balls represent Pt and CoO_x, respectively

respectively^{27,28}. The larger lattice distance of 0.350 nm matches well with (101) planes of anatase TiO₂²⁶. For the CoO_x/TiO₂/Pt catalyst (Fig. 2c, d), Pt nanoparticles (indicated by yellow circles) with an average particle size of 3.1 nm (Supplementary Fig. 3) are uniformly deposited on the inner surface of the TiO₂ nanotubes, while CoO_x nanoparticles are uniformly deposited on the outer surface of the TiO₂ nanotubes (Supplementary Fig. 4). In CoO_xPt/TiO₂ catalysts, the Pt nanoparticles are closely contacted with CoO_x nanoparticles, while in CoO_x/TiO₂/Pt catalysts, the

average CoO_x–Pt distance is corresponded to the TiO₂ thickness. Thus the average CoO_x–Pt distance in CoO_xPt/TiO₂ is much smaller than that of CoO_x/TiO₂/Pt. The sample was further characterized by using high-angle annular dark-field scanning TEM (HAADF-STEM), and energy-dispersive X-ray spectroscopy (EDS) mapping (Fig. 2e and Supplementary Figs. 5 and 6), further confirming that the Pt and CoO_x nanoparticles are separately decorated on the inner and outer surfaces of the TiO₂ nanotubes, respectively.

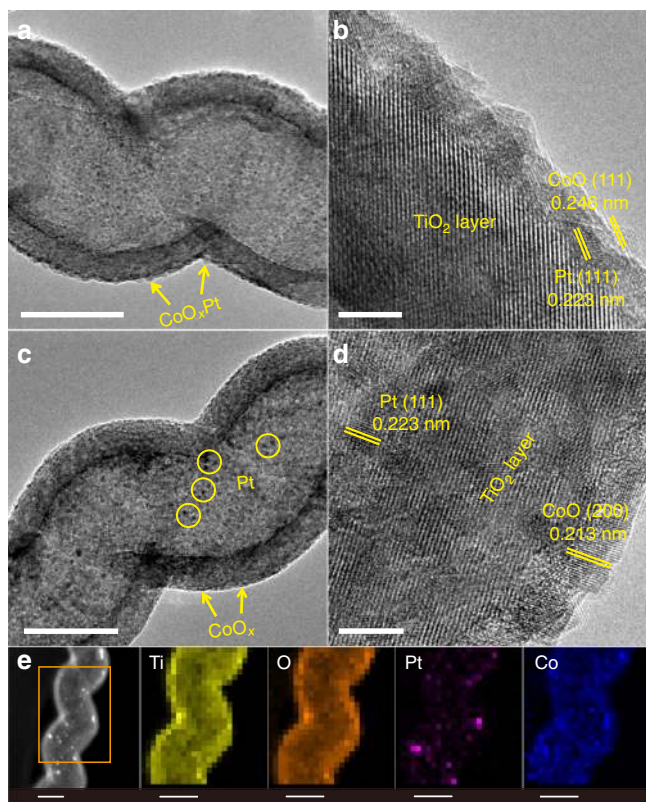


Fig. 2 Structural characterizations of the two catalysts. TEM and HRTEM images of the CoO_xPt/TiO₂ (**a, b**) and CoO_x/TiO₂/Pt (**c, d**) catalysts. **e** STEM image of the CoO_x/TiO₂/Pt catalysts and the corresponding EDS mapping profiles in rectangular area. Scale bars: **a, c** and **e** 50 nm; **b** and **d** 5 nm

Catalytic performance. The selective hydrogenation of C=O in α , β -unsaturated aldehydes (e.g., CALD) to value-added unsaturated alcohols has been of increasing interest for the production of fine chemicals and pharmaceutical precursors^{29–38}. However, it remains challenging to achieve high-yield unsaturated alcohols since the hydrogenation of C=C is thermodynamically more favorable than that of C=O. To address the issue, various catalysts have been designed and synthesized, and Pt-based catalysts were found to be more desirable in the selective reduction of C=O than other metals^{29–38}. Bitter and coworkers found that Pt particle size and oxygen groups on carbon nanofiber supports have a vital influence on the selectivity to cinnamyl alcohol (CALC)²⁹. Chen and coworkers reported that Co–Pt/SiO₂ bimetallic catalysts exhibit better catalytic activity and selectivity than Pt/SiO₂ and Cu–Pt/SiO₂ catalysts due to the electronic property modification of Pt^{30,31}. Similar results were also reported by Tsang et al., i.e., the selective C=O hydrogenation can be achieved with high activity using Co-decorated Pt nanocrystals as nanocatalysts³⁸.

To unravel the synergetic mechanism, the selective hydrogenation of CALD is selected as an example to evaluate the catalytic properties of the as-prepared catalysts, and the results are summarized in Table 1. Note that the Pt nanoparticles are located at different positions for the Pt/TiO₂ and TiO₂/Pt catalysts. For the monometallic TiO₂/Pt catalyst with Pt loading of 3.7 wt.% (Supplementary Table 1), the main product is hydrocinnamaldehyde (HALD) obtained from hydrogenation of the C=C and the selectivity to HALD amounts to 62.5%, while the selectivity to the desired product CALC, obtained from hydrogenation of the C=O, is only 16.2% (Entry 1). For the CoO_x/TiO₂ reference catalyst, only trace conversion (0.9%) is detected under the same reaction conditions (Entry 2). For the CoO_xPt/TiO₂ catalysts with closely contacted Pt and CoO_x, the selectivity to CALC is remarkably improved after addition of CoO_x (Entry 3). Moreover,

Table 1 Selective hydrogenation results of CALD over the different catalysts^a

| Entry | Catalysts | Conversion (%) (CALD) | Selectivity (%) | | |
|-------|---|-----------------------|-----------------|--------|--------|
| | | | (CALC) | (HALD) | (HALC) |
| 1 | TiO ₂ /Pt | 93.1 | 16.2 | 62.5 | 21.7 |
| 2 | CoO _x /TiO ₂ | 0.9 | – | – | – |
| 3 | CoO _x Pt/TiO ₂ | 92.4 | 82.1 | 14.5 | 3.3 |
| 4 | CoO _x /TiO ₂ /Pt | 91.3 | 81.5 | 13.9 | 4.3 |
| 5 | CoO _x /TiO ₂ (900)/Pt ^b | 89.8 | 80.3 | 14.3 | 4.7 |
| 6 | CoO _x /TiO ₂ /Pt/TiO ₂ | 8.8 | 52.1 | 47.4 | – |
| 7 | Al ₂ O ₃ /CoO _x /TiO ₂ /Pt ^c | 90.2 | 77.8 | 15.9 | 5.8 |
| 8 | Al ₂ O ₃ /Pt ^d | 31.8 | – | 100 | – |
| 9 | CoO _x /Al ₂ O ₃ /Pt | 18.5 | 39.1 | 60.7 | – |
| 10 | CoO _x Pt/Al ₂ O ₃ | 27.4 | 69.4 | 30.2 | – |
| 11 | CoO _x /Al ₂ O ₃ | 0.2 | – | – | – |

^aReaction conditions: 30 mL of 0.8 mmol cinnamaldehyde in ethanol and 2 MPa H₂ were placed in 50 mL stainless-steel autoclave (65 °C for 1.5 h)

^bThe cycle number of TiO₂ is 900 for the catalysts. For all other catalysts, the cycle number of TiO₂ is 300

^cDense Al₂O₃ layer is used to guarantee the complete covering of CoO_x species

^dThe cycle number of Al₂O₃ is 100 for the Al₂O₃-based catalysts (Entries 8–11)

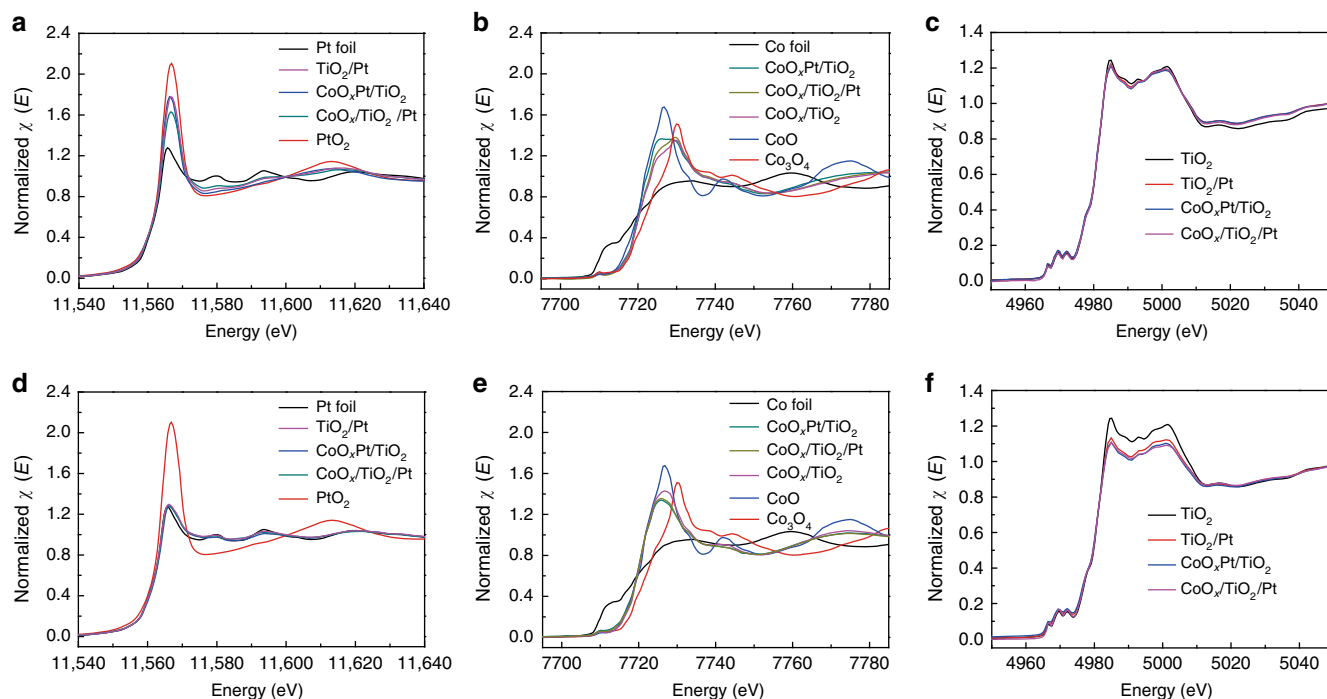


Fig. 3 XANES spectra of the catalysts. **a** Ex situ and **d** in situ Pt L₃-edge XANES spectra of TiO₂/Pt, CoO_x/TiO₂/Pt, CoO_xPt/TiO₂, and reference Pt foil and PtO₂; **b** Ex situ and **e** in situ Co K-edge XANES spectra of TiO₂/Pt, CoO_x/TiO₂/Pt, CoO_xPt/TiO₂, and reference Co foil, CoO and Co₃O₄; **c** Ex situ and **f** in situ Ti K-edge XANES spectra of TiO₂/Pt, CoO_xPt/TiO₂, CoO_x/TiO₂/Pt and reference TiO₂

the product of excessive hydrogenation to hydrocinnamyl alcohol (HALC) is also obviously suppressed. Similar phenomenon is also found for the CoO_x-supported Pt-based catalysts, and the Pt₄₀/CoO_x catalysts exhibit the best catalytic performance with 90.2% conversion and 80.3% selectivity to CALC (Supplementary Fig. 7). The improved selectivity to CALC is usually ascribed to the promoter effects, originating from electronic or structural modifications^{35–41}. Unexpectedly, similar hydrogenation results are also achieved over the CoO_x/TiO₂/Pt (13.7 nm, 300-cycle TiO₂) catalysts with nanoscale CoO_x-Pt intimacy (Entry 4 and Supplementary Fig. 8). Moreover, only slight decrease in hydrogenation activity and selectivity is observed over the CoO_x/TiO₂(900)/Pt catalysts (Entry 5) when the TiO₂ layer becomes much thicker (40.5 nm, 900-cycle TiO₂, Supplementary Figs. 9 and 10).

Furthermore, control experiments were also carried out by selectively exposing Pt or CoO_x to confirm the roles played by CoO_x and Pt during the reaction. The hydrogenation conversion and selectivity to the desired CALC product decrease remarkably when Pt is selectively covered by two-layered TiO₂ (CoO_x/TiO₂/Pt/TiO₂, Entry 6). When CoO_x is selectively covered by an outer dense Al₂O₃ layer of ~11.5 nm (Al₂O₃/CoO_x/TiO₂/Pt), no visible change is observed in the catalytic performance (Entry 7). These results indicate that Pt–TiO₂ interface regions should be the main active sites for the CALD hydrogenation reaction, instead of CoO_x. It should be noted that the selectivity of CALC hydrogenation is guaranteed to improve with CoO_x addition due to the long-range promoter effect and that this effect is not broken even when the surface of CoO_x promoter is entirely covered by a dense Al₂O₃ layer (Al₂O₃/CoO_x/TiO₂/Pt, Entry 7). This effect is altered when the TiO₂ layer is changed to Al₂O₃ (~11.5 nm), i.e., the catalytic performance is considerably influenced by the CoO_x–Pt intimacy (Entries 8–11). Closely contacted CoO_xPt/Al₂O₃ catalysts exhibit higher activity and selectivity to the desired product than those of the separated CoO_x/Al₂O₃/Pt catalysts with nanoscale intimacy. This should be

related to the poor capability of spillover hydrogen transfer on the nonreducible Al₂O₃⁷. In addition, the reusability of CoO_x/TiO₂/Pt for selective hydrogenation of CALD was also tested (Supplementary Fig. 11). There is no obvious decrease in the conversion after five catalytic cycles, indicating a good stability of the catalysts.

X-ray absorption fine structure measurements. The electronic states of the TiO₂/Pt, CoO_x/TiO₂/Pt and CoO_xPt/TiO₂ catalysts before and during the hydrogenation reaction processes were investigated by ex situ and in situ X-ray absorption fine structure measurements (Fig. 3). Figure 3a shows the normalized Pt L₃-edge ex situ X-ray absorption near-edge structure (XANES) spectra of the as-prepared catalysts, and the reference spectra of Pt foil and PtO₂. The white line intensity of the as-prepared catalysts falls in the range between the Pt foil and PtO₂, suggesting that the as-prepared Pt nanoparticles consist of a certain amount of PtO_x in addition to metallic Pt⁰. Expanded view of the white lines (Supplementary Fig. 12) indicates the different electronic states of Pt for TiO₂/Pt, CoO_x/TiO₂/Pt and CoO_xPt/TiO₂ catalysts. Figure 3b presents the normalized Co K-edge XANES spectra of the as-prepared catalysts before the reaction, and the reference spectra of Co foil, CoO and Co₃O₄. Obviously, the CoO_x/TiO₂/Pt catalysts also exhibit different white line shapes in comparison with the CoO_xPt/TiO₂ catalysts, indicating the different electronic states of the CoO_x species between the two catalysts. These results demonstrate that before the reaction, the electronic interaction between CoO_x promoter and Pt should exist (Supplementary Fig. 13). During the reaction process, the PtO_x species of TiO₂/Pt, CoO_x/TiO₂/Pt and CoO_xPt/TiO₂ are fully reduced to metallic Pt⁰ due to the presence of H₂ (Fig. 3d). The Fourier transform spectra of the Pt L₃-edge extended X-ray absorption fine structure (EXAFS) oscillations for these three catalysts also confirm the full reduction of PtO_x during the reaction process (Supplementary Fig. 14a, b). For the CoO_x/TiO₂ reference catalysts, the white line shifts to a low energy during the

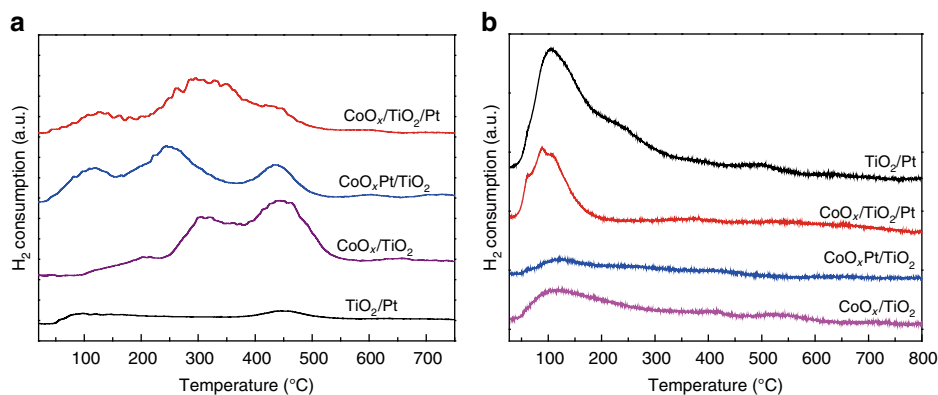


Fig. 4 Chemisorption characterizations. **a** H_2 -TPR and **b** H_2 -TPD profiles of the catalysts

reaction process (Fig. 3b and e), indicating that the cobalt oxide species at high valence could be reduced to relatively low valence states (e.g., from Co_3O_4 to CoO) under a H_2 atmosphere without Pt assistance (Supplementary Fig. 14c, d). Lower energy shifts of the white lines can be observed for the CoO_xPt/TiO_2 and $CoO_x/TiO_2/Pt$ catalysts during the reaction process, demonstrating that more cobalt oxide species with lower valence states are formed in the two catalysts compared with the CoO_x/TiO_2 catalysts, which can be ascribed to the presence of Pt contributing to the reduction of CoO_x due to the hydrogen spillover effect. In addition, the CoO_xPt/TiO_2 and $CoO_x/TiO_2/Pt$ catalysts exhibit almost the same white line shapes during the reaction process (Fig. 3e), i.e., the valence states of the formed cobalt oxide species of the two catalysts are nearly identical; this is due to the strong reduction ability of the spillover hydrogen ($H\cdot$), generated on Pt, toward CoO_x , which is nearly independent of the CoO_x -Pt intimacy on reducible TiO_2 supports in the nanoscale range⁷.

Figure 3c and f shows the normalized Ti K-edge ex situ and in situ XANES spectra of TiO_2/Pt , $CoO_x/TiO_2/Pt$, CoO_xPt/TiO_2 and the reference spectra of TiO_2 . Before the reaction, the Ti K-edge white line curves of all the three catalysts coincide, indicating the same electronic states of their TiO_2 supports. During the hydrogenation reaction conditions, in situ XANES spectra show reduction of Ti^{4+} to Ti^{3+} for all three catalysts, and $CoO_x/TiO_2/Pt$ and CoO_xPt/TiO_2 possess more reduced Ti^{3+} than that of the TiO_2/Pt catalyst. The k^3 -weighted EXAFS spectra of the three catalysts and the reference TiO_2 , and their fitted curves are presented in Supplementary Fig. 15. The fitted results (Supplementary Table 2) are consistent with the XANES results.

Chemisorption. Figure 4a shows the H_2 temperature programmed reduction (H_2 -TPR) profiles of the catalysts. From the H_2 -TPR profiles of the CoO_xPt/TiO_2 , $CoO_x/TiO_2/Pt$ and CoO_x/TiO_2 catalysts (also see Supplementary Fig. 10), both a low temperature (110–220 °C, Co_3O_4 to CoO) and a high temperature (245–345 °C, CoO to Co^0) reduction peak can be observed. No peaks related to platinum oxides are observed, probably because the amounts of H_2 used for the reduction of PtO_x species in the catalysts are beyond the lower detection limits of the detector. In addition, the reduction peak at higher temperature (~450 °C) could be assigned to the partial reduction of TiO_2 , indicating that TiO_2 is more difficult to reduce⁴². Compared with the CoO_x/TiO_2 catalysts, the temperatures needed for CoO_x reduction are much lower for the CoO_xPt/TiO_2 and $CoO_x/TiO_2/Pt$ catalysts due to the presence of Pt, further revealing the effect of hydrogen spillover from Pt to CoO_x ³¹. Note that the reduction temperature needed for the CoO_xPt/TiO_2 catalyst is slightly lower than that of the $CoO_x/TiO_2/Pt$ catalyst due to the closer CoO_x -Pt intimacy

(Fig. 4a). Figure 4b shows the H_2 temperature programmed desorption (H_2 -TPD) profiles of the catalysts. The TiO_2/Pt and $CoO_x/TiO_2/Pt$ catalysts exhibit a much higher H_2 adsorption ability than that of the CoO_x/TiO_2 and CoO_xPt/TiO_2 catalysts, indicating that Pt atoms are the adsorption and dissociation sites of H_2 , which is further verified by the following density functional theory (DFT) simulation.

Discussion

In this work, we discovered a hydrogen spillover effect for the CALD hydrogenation reactions. Hydrogen spillover is a reversible and dynamic equilibrium process. Modulation of the spillover conditions, such as temperature and gas partial pressure, hinders or facilitates the spillover process and can be used for controlling the oxide reduction^{7,43}. Generally, the activation and dissociation of H_2 molecules on Pt is quite easy and generally considered to be barrierless^{7,43–45}, i.e., the energy needed to activate H_2 molecules on Pt is much lower than that on CoO_x and TiO_2 (Supplementary Fig. 16). For the TiO_2/Pt catalyst under the reaction conditions, hydrogen spillover occurs (Fig. 5a). Active hydrogen species migrate from Pt onto TiO_2 supports, leading to the partial reduction of TiO_2 supports (Ti^{4+} is reduced to Ti^{3+}) with the formation of O_v around the interface regions^{7,46–50}. When CoO_x is added, in situ XAFS results show that CoO_x can be reduced to lower valent states through hydrogen spillover under the reaction conditions. More hydrogen species are consumed by CoO_x , thus the original equilibrium of hydrogen spillover is disturbed (Fig. 5a). The generation of active hydrogen species and their transfer process (from Pt to CoO_x directly, or via TiO_2 supports) are promoted, until new equilibrium is reached. The consumption of hydrogen species can be seen as the pumps for the migration of atomic hydrogen from Pt toward TiO_2 . The enhanced hydrogen spillover facilitates the reduction of TiO_2 supports, which is proved by in situ Ti K-edge XANES spectra (Fig. 3c and f), accompanying the increased formation of O_v sites.

The adsorption energies of different adsorption configurations of a CALD molecule on the O_v formed on TiO_2 were calculated (Fig. 5b). The calculated adsorption energy of the C=O bond adsorbed on the oxygen vacancies is -2.38 eV, which is larger than that of the C=C bond on the oxygen vacancies (-1.68 eV), indicating that the adsorption configurations of the CALD molecule through the C=O bond on the O_v are more stable.

Based on the above discussions, the possible enhancement mechanism is proposed. For the TiO_2/Pt catalyst, the number of O_v at the Pt- TiO_2 interface is limited under the reaction conditions, leading to its low selectivity (Fig. 5c). When CoO_x promoters are added, the selectivity to CALC is improved. The promotion can be ascribed to the CoO_x promoter-induced

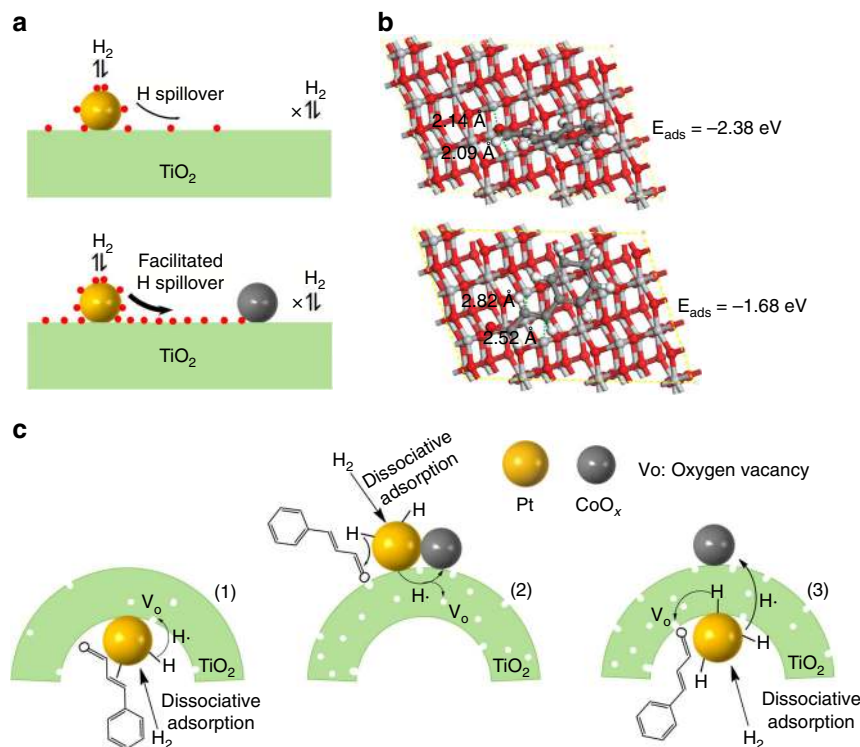


Fig. 5 DFT calculation and proposed reaction mechanisms. **a** The effect mechanism of CoO_x on the hydrogen spillover over TiO₂-supported Pt catalysts. **b** The optimized structure for adsorption of CALD molecule using C=O (top) or C=C (bottom) double bond on the O_v of TiO₂. Atom coloring: Ti, gray; O, red; H, white; C, black. **c** The possible enhancement mechanism for selective CALD hydrogenation reaction. (1), (2) and (3) represent TiO₂/Pt, CoO_xPt/TiO₂ and CoO_x/TiO₂/Pt catalysts, respectively. For TiO₂/Pt, the number of O_v is limited, leading to its low selectivity. For CoO_xPt/TiO₂ and CoO_x/TiO₂/Pt, the addition of CoO_x promotes the formation of O_v sites through hydrogen spillover and thus improves the selectivity, regardless of whether CoO_x and Pt are separated by a TiO₂ layer or not

increase of O_v sites through hydrogen spillover effect. For CoO_x/TiO₂/Pt catalysts, although CoO_x is separated from the Pt catalyst by a TiO₂ layer, this long-range CoO_x promoter can still enhance the catalytic selectivity to CALC. XAFS results demonstrate that the electronic states of CoO_x of CoO_xPt/TiO₂ and CoO_x/TiO₂/Pt catalysts are almost the same during the reaction process, meaning that the active hydrogen species generated on Pt nanoparticles are still consumed by CoO_x, though CoO_x is far from Pt. The energy barrier for the transfer of an electron and a proton among the different TiO₂ sites can be easily overcome under the reaction conditions⁷, and thus the distance of hydrogen spillover across TiO₂ layer almost has no influence on the catalytic performance. The addition of CoO_x results in the increased generation of O_v sites on the Pt-TiO₂ interface regions and the remarkably improved selectivity to CALC.

To further clarify the long-range promoter effect (i.e., the role of CoO_x played), we selectively deposit additional oxide layers on the surfaces of CoO_x or Pt by ALD. From the XAFS results, it can be concluded that CoO_x species in the catalysts can be reduced in two ways. Firstly, the CoO_x species can be reduced under H₂ atmosphere; secondly, the CoO_x species can be further reduced to a lower valence state by the active H species spilled from Pt nanoparticles through TiO₂ support. When Pt is selectively covered by TiO₂ (CoO_x/TiO₂/Pt/TiO₂), the access of CALD molecules to Pt is nearly blocked due to the diffusion limitation (Supplementary Figs. 17 and 18, Supplementary Table 3), leading to the decreased catalytic performance (Entry 6, Table 1). On the contrary, when CoO_x is selectively covered by a dense Al₂O₃ layer (Al₂O₃/CoO_x/TiO₂/Pt), the first way is blocked (Supplementary Fig. 18), while the second way is still preserved and CALD molecules can still have access to Pt via open the ends of the TiO₂

nanotubes (with a diameter of ~70–90 nm), leading to a nearly unchanged catalytic performance (Entry 7, Table 1). These results further demonstrate that H spillover way is the main path to improve selectivity, and that Pt–O_v interface instead of CoO_x should be the active site for the CALD hydrogenation reaction.

In summary, we have successfully developed a general method based on template-assisted ALD to synthesize closely contacted CoO_xPt/TiO₂ and spatially separated CoO_x/TiO₂/Pt catalysts, achieving the precise tuning of CoO_x–Pt intimacy by varying the deposition sequence and the wall thickness of the TiO₂ nanotubes. We discover that hydrogen spillover effect generated by the addition of CoO_x can cause the increase in O_v, providing the adsorption sites for CALD via C=O bond and correspondingly resulting in the enhancement of selectivity to CALC in the CALD hydrogenation reactions. This hydrogen spillover effect is not broken even when we selectively deposit additional oxide layers on the CoO_x promoter by ALD to cover its surface entirely. Our work has demonstrated an efficient strategy based on ALD for the design of various bicomponent catalysts with distinct promoter–metal intimacy and the assembly of metals and oxide supports, which is helpful to reveal the origin of bicomponent synergy, the enhancement mechanism and the real active sites.

Methods

Synthesis of CNCs and the ALD process. The detailed CNC synthesis process and the ALD process can be found in our previous reports^{24–26}.

Synthesis of TiO₂/Pt catalysts. CNCs were firstly decorated with Pt nanoparticles by Pt ALD (20 cycles) and then coated with a TiO₂ layer (300 cycles) by TiO₂ ALD, producing TiO₂/Pt/CNCs. After the ALD processes, TiO₂/Pt/CNCs were calcinated at 500 °C for 2 h in air to remove the CNC templates, obtaining TiO₂/Pt catalysts, in which Pt nanoparticles were confined in TiO₂ nanotubes.

Synthesis of CoO_x/TiO₂/Pt catalysts. The above-obtained TiO₂/Pt catalysts were then deposited with cobalt oxides (denoted as CoO_x) by CoO_x ALD (150 cycles), obtaining shell-isolated CoO_x/TiO₂/Pt catalysts.

Synthesis of CoO_xPt/TiO₂ catalysts. CNCs were firstly coated with a TiO₂ amorphous film by TiO₂ ALD, and then Pt nanoparticles were deposited on the TiO₂/CNCs by Pt ALD obtaining Pt/TiO₂/CNCs composites. Subsequently, CNCs were removed by calcination under an air atmosphere producing Pt/TiO₂ catalysts with porous anatase nanotubes. Lastly, CoO_x nanoparticles were deposited on the outer surface of Pt/TiO₂ through CoO_x ALD, producing CoO_xPt/TiO₂ catalysts with the closest CoO_x-Pt intimacy.

Synthesis of CoO_x/TiO₂/Pt/TiO₂ catalysts. CNCs were first coated with a TiO₂ layer (150 cycles) by TiO₂ ALD and then decorated with Pt nanoparticles by Pt ALD and another TiO₂ layer (300 cycles) producing TiO₂/Pt/TiO₂/CNCs. After the ALD processes, TiO₂/Pt/TiO₂/CNCs were calcinated at 500 °C for 2 h in air to remove the CNC templates, obtaining sandwich-like TiO₂/Pt/TiO₂ catalysts, in which Pt nanoparticles are coated by the two-layer TiO₂. Lastly, the obtained TiO₂/Pt/TiO₂ catalysts were decorated with CoO_x nanoparticles by CoO_x ALD producing CoO_x/TiO₂/Pt/TiO₂.

Synthesis of Al₂O₃/CoO_x/TiO₂/Pt catalysts. CNCs were sequentially decorated with Pt nanoparticles by CoO_x ALD, coated with a TiO₂ layer (300 cycles) by TiO₂ ALD, decorated with Pt nanoparticles by Pt ALD and then coated with an Al₂O₃ layer (100 cycles) by Al₂O₃ ALD producing Al₂O₃/CoO_x/TiO₂/Pt/CNCs, which were calcinated at 550 °C for 2 h in air to remove the CNC templates obtaining Al₂O₃/CoO_x/TiO₂/Pt catalysts, in which CoO_x nanoparticles were covered by the outer Al₂O₃ layer.

Catalyst characterizations. TEM and HRTEM images were taken with a JEOL-2100F field-emission transmission electron microscope operated at 200 kV. HAADF-STEM images and EDS mapping profiles were collected on a JEOL ARM-200F field-emission transmission electron microscope operated at 200 kV. The X-ray diffraction (XRD) patterns were recorded by using a Philips X'Pert Pro Super X-ray diffractometer with Cu K α radiation ($\lambda = 1.540 \text{ \AA}$) in the 2θ range from 10° to 90°. The X-ray photoelectron spectra (XPS) were collected on an ESCALAB-250 X-ray photoelectron spectrometer with an Al K α source (1486.6 eV). The XANES and EXAFS spectra of the Pt L₃-edge and Co K-edge were measured on the BL14W1 beamline of the Shanghai Synchrotron Radiation Facility (SSRF), Shanghai Institute of Applied Physics (SINAP), China, operated at 3.5 GeV. A Si (111) double-crystal monochromator was used to reduce the harmonic component of the monochrome beam. Pt foil, PtO₂, Co foil, CoO and Co₃O₄ were used as reference samples and measured in the transmission mode, and all the catalysts were also measured in the transmission mode. The diffuse reflectance infrared Fourier transform spectroscopy (DRIFTS, CO chemisorption) measurements were performed on a Bruker Vector 22 spectrometer. After the sample was loaded, it was firstly reduced by 10% H₂/Ar at 150 °C for 1.5 h. Then the sample was cooled to 30 °C under 10% H₂/Ar atmosphere, on which a background spectrum was collected. Subsequently, CO was introduced onto the sample until saturation, followed by Ar purge to remove the physically adsorbed gaseous CO. Finally, CO-DRIFTS spectra were collected with 250 scans. H₂-TPR experiments were performed in a tubular quartz reactor (TP-5080, Tianjin Xianquan, China), into which 50 mg sample was loaded. The reduction was conducted in a 10% H₂/N₂ atmosphere at a heating rate of 10 °C/min. H₂-TPD experiments were performed in the same apparatus. A 50-mg sample was firstly reduced in situ at 250 °C for 1 h in a 10% H₂/N₂ flow and then cooled to 30 °C in the same atmosphere. Subsequently, the sample was swept with nitrogen at a flow rate of 30 sccm for 30 min to remove physisorbed or weakly bound species. TPD was performed by heating the sample from room temperature to 800 °C at a ramp rate of 10 °C/min in nitrogen. N₂ adsorption-desorption experiments were performed on a BELSORP-Mini system at 77 K. The specific surface area was determined using the Brunauer-Emmett-Teller (BET) method, and the pore size distributions were calculated by the Barrett-Joyner-Halenda (BJH) method according to the desorption branches. The Pt and Co metal content of the samples was determined by inductively coupled plasma mass spectrometry (ICP-MS) analysis (Thermo ICAP 6300).

Catalytic activity measurements. CALD hydrogenation reactions were performed on the above catalysts in a 50-mL stainless-steel autoclave reactor. The reaction was carried out at 65 °C and 2.0 MPa H₂ with a certain amount of catalysts in 30 mL of ethanol, and 100 μ L of CALD. After the reaction, the reactor was cooled and then slowly depressurized. Finally, the reaction mixture was separated by centrifugation in order to remove the solid catalysts. The reaction products were analyzed and quantified by gas chromatographic mass spectrometry (GC-MS, Agilent, 7890A). The reaction conversion and selectivity were determined by the product analysis.

Computational method. Periodic DFT calculations within the generalized gradient approximation (GGA) were conducted with the Vienna ab initio Simulation

Package (VASP 5.3.5) with considering the spin-polarization, in which a projector-augmented potential (PAW) method is implemented. The Perdew-Burke-Ernzerhof (PBE) functional at the GGA level was used, and the plane wave basis set was cut off at the energy of 400 eV. For our ALD-prepared cobalt-based catalysts, the obtained cobalt oxides consist of Co₃O₄ and CoO and the main species is CoO. Therefore, CoO was selected for DFT calculations. The CoO surface was modeled with a six GGA extension atomic layer 3 \times 3 CoO(111) slab. DFT + U corrections (an effective onsite Coulomb interaction parameter) were employed to mitigate the self-interaction errors of Co 3d orbital with U-J of 7.1 eV. The main exposed crystal plane for ALD-prepared TiO₂ is the thermodynamically most stable (101) surface, and thus (101) surface was chosen as a model for the anatase TiO₂ interface. The TiO₂ surface was modeled with a six atomic layer 3 \times 3 slab. The slab and its image were separated by a vacuum region of 15 \AA . The reactant molecular and the top two layers of these model systems were relaxed, whereas other atoms were fixed in their initial lattice sizes.

Data availability

All the relevant data are available from the authors upon request.

Received: 5 December 2018 Accepted: 14 August 2019

Published online: 13 September 2019

References

1. Tao, F. F. Synthesis, catalysis, surface chemistry and structure of bimetallic nanocatalysts. *Chem. Soc. Rev.* **41**, 7977–7979 (2012).
2. Sankar, M. et al. Designing bimetallic catalysts for a green and sustainable future. *Chem. Soc. Rev.* **41**, 8099–8139 (2012).
3. Behrens, M. et al. Performance improvement of nanocatalysts by promoter-induced defects in the support material: methanol synthesis over Cu/ZnO:Al. *J. Am. Chem. Soc.* **135**, 6061–6068 (2013).
4. Briggs, N. M. et al. Identification of active sites on supported metal catalysts with carbon nanotube hydrogen highways. *Nat. Commun.* **9**, 3827 (2018).
5. Phaahlamohla, T. N. et al. Effects of Co and Ru intimacy in Fischer-Tropsch catalysts using hollow carbon sphere supports: assessment of the hydrogen spillover processes. *ACS Catal.* **7**, 1568–1578 (2017).
6. Zhang, H. et al. Revealing the role of interfacial properties on catalytic behaviors by in situ surface-enhanced raman spectroscopy. *J. Am. Chem. Soc.* **139**, 10339–10346 (2017).
7. Karim, W. et al. Catalyst support effects on hydrogen spillover. *Nature* **541**, 68–71 (2017).
8. Samad, J. E., Blanchard, J., Sayag, C., Louis, C. & Regalbutto, J. R. The controlled synthesis of metal-acid bifunctional catalysts: the effect of metal: acid ratio and metal-acid proximity in Pt silica-alumina catalysts for n-heptane isomerization. *J. Catal.* **342**, 203–212 (2016).
9. Cheng, K. et al. Direct and highly selective conversion of synthesis gas into lower olefins: design of a bifunctional catalyst combining methanol synthesis and carbon-carbon coupling. *Angew. Chem. Int. Ed. Engl.* **128**, 4803–4806 (2016).
10. Gläser, R. Catalysis: the complexity of intimacy. *Nature* **528**, 197–198 (2015).
11. Lu, J., Elam, J. W. & Stair, P. C. Synthesis and stabilization of supported metal catalysts by atomic layer deposition. *Acc. Chem. Res.* **46**, 1806–1815 (2013).
12. Lee, H.-B.-R. & Bent, S. F. Formation of continuous Pt films on the graphite surface by atomic layer deposition with reactive O₃. *Chem. Mater.* **27**, 6802–6809 (2015).
13. O'Neill, B. J. et al. Catalyst design with atomic layer deposition. *ACS Catal.* **5**, 1804–1825 (2015).
14. Liu, X. et al. Oxide-nanotrap-anchored platinum nanoparticles with high activity and sintering resistance by area-selective atomic layer deposition. *Angew. Chem. Int. Ed. Engl.* **129**, 1670–1674 (2017).
15. Meng, X. et al. Atomic layer deposition for nanomaterial synthesis and functionalization in energy technology. *Mater. Horiz.* **4**, 133–154 (2017).
16. Gao, Z. & Qin, Y. Design and properties of confined nanocatalysts by atomic layer deposition. *Acc. Chem. Res.* **50**, 2309–2316 (2017).
17. Dendooven, J. et al. Independent tuning of size and coverage of supported Pt nanoparticles using atomic layer deposition. *Nat. Commun.* **8**, 1074 (2017).
18. Lu, J. et al. Coking- and sintering-resistant palladium catalysts achieved through atomic layer deposition. *Science* **335**, 1205–1208 (2012).
19. Zhang, J. et al. Highly dispersed Pt nanoparticles supported on carbon nanotubes produced by atomic layer deposition for hydrogen generation from hydrolysis of ammonia borane. *Catal. Sci. Technol.* **7**, 322–329 (2017).
20. Gould, T. D. et al. Controlling nanoscale properties of supported platinum catalysts through atomic layer deposition. *ACS Catal.* **5**, 1344–1352 (2015).
21. Cheng, N. et al. Platinum single-atom and cluster catalysis of the hydrogen evolution reaction. *Nat. Commun.* **7**, 13638 (2016).

22. Van Bui, H., Grillo, F., Helmer, R., Goulas, A. & van Ommen, J. R. Controlled growth of palladium nanoparticles on graphene nanoplatelets via scalable atmospheric pressure atomic layer deposition. *J. Phys. Chem. C* **120**, 8832–8840 (2016).
23. Wang, X. et al. Atomic layer deposited Pt-Co bimetallic catalysts for selective hydrogenation of α,β -unsaturated aldehydes to unsaturated alcohols. *J. Catal.* **366**, 61–69 (2018).
24. Gao, Z. et al. Multiply confined nickel nanocatalysts produced by atomic layer deposition for hydrogenation reactions. *Angew. Chem. Int. Ed. Engl.* **54**, 9006–9010 (2015).
25. Ge, H. et al. A tandem catalyst with multiple metal oxide interfaces produced by atomic layer deposition. *Angew. Chem. Int. Ed. Engl.* **128**, 7197–7201 (2016).
26. Zhang, J. et al. Porous TiO₂ nanotubes with spatially separated platinum and CoO_x cocatalysts produced by atomic layer deposition for photocatalytic hydrogen production. *Angew. Chem. Int. Ed. Engl.* **56**, 816–820 (2017).
27. Ramachandran, R. K. et al. Atomic layer deposition route to tailor nanoalloys of noble and non-noble metals. *ACS Nano* **10**, 8770–8777 (2016).
28. Mao, S. et al. High-performance bi-functional electrocatalysts of 3D crumpled graphene-cobalt oxide nanohybrids for oxygen reduction and evolution reactions. *Energy Environ. Sci.* **7**, 609–616 (2014).
29. Plomp, A. J. et al. Particle size effects for carbon nanofiber supported platinum and ruthenium catalysts for the selective hydrogenation of cinnamaldehyde. *Appl. Catal. A Gen.* **351**, 9–15 (2008).
30. Yu, W., Porosoff, M. & Chen, J. G. Review of Pt-based bimetallic catalysis: from model surfaces to supported catalysts. *Chem. Rev.* **112**, 5780–5817 (2012).
31. Zheng, R. et al. Controlling hydrogenation of C=O and C=C bonds in cinnamaldehyde using silica supported Co-Pt and Cu-Pt bimetallic catalysts. *Appl. Catal. A Gen.* **419–420**, 126–132 (2012).
32. Nongwe, I. et al. Pt supported nitrogen doped hollow carbon spheres for the catalysed reduction of cinnamaldehyde. *Appl. Catal. A Gen.* **517**, 30–38 (2016).
33. Wu, B. et al. Selective hydrogenation of α,β -unsaturated aldehydes catalyzed by amine-capped platinum-cobalt nanocrystals. *Angew. Chem. Int. Ed. Engl.* **51**, 3440–3443 (2012).
34. Ji, X. et al. Selective hydrogenation of cinnamaldehyde to cinnamal alcohol over platinum/graphene catalysts. *ChemCatChem* **6**, 3246–3253 (2014).
35. Wang, H. et al. A strongly coupled ultrasmall Pt₃Co nanoparticle-ultrathin Co(OH)₂ nanosheet architecture enhances selective hydrogenation of α,β -unsaturated aldehydes. *ACS Catal.* **9**, 154–159 (2019).
36. Li, C. et al. The remarkable promotion of in situ formed Pt-cobalt oxide interfacial sites on the carbonyl reduction to allylic alcohols. *Mol. Catal.* **455**, 78–87 (2018).
37. Guo, Z. et al. Carbon nanotube-supported Pt-based bimetallic catalysts prepared by a microwave-assisted polyol reduction method and their catalytic applications in the selective hydrogenation. *J. Catal.* **276**, 314–326 (2010).
38. Tsang, S. C. et al. Engineering preformed cobalt-doped platinum nanocatalysts for ultraselective hydrogenation. *ACS Nano* **2**, 2547–2553 (2008).
39. Kennedy, G., Melaet, G., Han, H.-L., Ralston, W. T. & Somorjai, G. A. In situ spectroscopic investigation into the active sites for crotonaldehyde hydrogenation at the Pt nanoparticle-Co₃O₄ interface. *ACS Catal.* **6**, 7140–7147 (2016).
40. Zhao, M. et al. Metal-organic frameworks as selectivity regulators for hydrogenation reactions. *Nature* **539**, 76–80 (2016).
41. Zheng, R., Zhu, Y. & Chen, J. G., Promoting low-temperature hydrogenation of C=O bonds of acetone and acetaldehyde by using Co-Pt bimetallic catalysts. *ChemCatChem* **3**, 578–581 (2011).
42. Zhu, Y., Liu, D. & Meng, M. H₂ spillover enhanced hydrogenation capability of TiO₂ used for photocatalytic splitting of water: a traditional phenomenon for new applications. *Chem. Commun.* **50**, 6049–6051 (2014).
43. Spreafico, C. et al. Hydrogen adsorption on nanosized platinum and dynamics of spillover onto alumina and titania. *J. Phys. Chem. C* **121**, 17862–17872 (2017).
44. Kyriakou, G. et al. Isolated metal atom geometries as a strategy for selective heterogeneous hydrogenations. *Science* **335**, 1209–1212 (2012).
45. Zhan, G. & Zeng, H. Hydrogen spillover through Matryoshka-type (ZIFs@)_n-ZIFs nanocubes. *Nat. Commun.* **9**, 3778 (2018).
46. Prins, R. Hydrogen spillover. Facts and fiction. *Chem. Rev.* **112**, 2714–2738 (2012).
47. Im, J. et al. Maximizing the catalytic function of hydrogen spillover in platinum-encapsulated aluminosilicates with controlled nanostructures. *Nat. Commun.* **5**, 3370 (2014).
48. Ruiz Puigdollers, A., Schlexer, P., Tosoni, S. & Pacchioni, G. Increasing oxide reducibility: the role of metal/oxide interfaces in the formation of oxygen vacancies. *ACS Catal.* **7**, 6493–6513 (2017).
49. Conner, W. C. Jr & Falconer, J. L. Spillover in heterogeneous catalysis. *Chem. Rev.* **95**, 759–788 (1995).
50. An, K. et al. Enhanced CO oxidation rates at the interface of mesoporous oxides and Pt nanoparticles. *J. Am. Chem. Soc.* **135**, 16689–16696 (2013).

Acknowledgements

We acknowledge the financial support from the National Natural Science Foundation of China (21773282, U1832208 and 21673269), National Science Fund for Distinguished Young Scholars (21825204), the National Key R&D Program of China (2017YFA0700101), Natural Science Foundation of Shanxi Province (201801D211011), Excellent Youth Scholars of State Key Laboratory of Coal Conversion (2016BWZ004), Youth Innovation Promotion Association of the Chinese Academy of Sciences (2018208) and National Postdoctoral Program for Innovative Talents (BX20180323). We are grateful to Shanghai Institute of Applied Physics for the X-ray absorption spectroscopy measurement.

Author contributions

J.Z. synthesized the catalysts and performed the activity tests. S.W. performed the theoretical calculation. G.W. helped to perform the XAFS measurement. X.G., B.Z., S.X. and S.Z. assisted in the synthesis and characterizations of the catalysts. Z.G. and Y.Q. conceived the idea and supervised the work. J.Z., Z.G. and Y.Q. wrote the manuscript. All authors contributed to the manuscript.

Additional information

Supplementary Information accompanies this paper at <https://doi.org/10.1038/s41467-019-11970-8>.

Competing interests: The authors declare no competing interests.

Reprints and permission information is available online at <http://npg.nature.com/reprintsandpermissions/>

Peer review information *Nature Communications* thanks Neil Coville and other, anonymous, reviewer(s) for their contribution to the peer review of this work.

Publisher's note Springer Nature remains neutral with regard to jurisdictional claims in published maps and institutional affiliations.



Open Access This article is licensed under a Creative Commons Attribution 4.0 International License, which permits use, sharing, adaptation, distribution and reproduction in any medium or format, as long as you give appropriate credit to the original author(s) and the source, provide a link to the Creative Commons license, and indicate if changes were made. The images or other third party material in this article are included in the article's Creative Commons license, unless indicated otherwise in a credit line to the material. If material is not included in the article's Creative Commons license and your intended use is not permitted by statutory regulation or exceeds the permitted use, you will need to obtain permission directly from the copyright holder. To view a copy of this license, visit <http://creativecommons.org/licenses/by/4.0/>.

© The Author(s) 2019